Section 4

Parameterization of atmospheric and surface processes, effects of different physical parameterizations.

High-Resolution Numerical Simulation of Wintertime Orographic Precipitation: Representation of Snowfall Characteristics

Kentaro Araki[1]

1: Meteorological Research Institute, Tsukuba, Ibaraki, Japan

e-mail: araki@mri-jma.go.jp

1. Introduction

In winter, surface avalanches often occur when extratropical cyclones moving along the south coast of Japan bring short-duration heavy snowfalls in mountain regions. Araki (2018) investigated the snowfall characteristics and meteorological conditions of a surface avalanche event in Nasu, Tochigi Prefecture, Japan on 27 March 2017. From the results of numerical simulation by the Japan Meteorological Agency (JMA) Non-Hydrostatic Model (NHM) with a horizontal grid spacing of 250 m, it is indicated that low-level supercooled water clouds were formed by orographically forced updrafts in mountainous regions in Nasu as moist northerly and easterly flows intensified due to the cyclone's approach. They suggested that localized snowfall intensification and short-duration heavy snowfalls were produced by the Seeder-Feeder mechanism associated with the low-level clouds and snow from the upper clouds of the cyclone. To forecast the potential of surface avalanches with leading time of 0.5-1 days, it is important to understand representations of the snowfall intensification by numerical weather models with different horizontal resolutions. In this study, we performed a case study on this surface avalanche event and examined model representations of snowfall characteristics at the horizontal resolutions from 250 m to 5 km.

2. Model settings

Numerical simulations were performed by the NHM with a domain covering Nasu and a horizontal grid spacing of 5 km (5km-NHM), 2 km (2km-NHM), 1 km, 500 m (500m-NHM), 250 m (250m-NHM). Detail of the description of each model is shown in Table 1. For the experiments with horizontal resolution of 1 km, both Mellor-Yamada-Nakanishi-Niino (1km-NHM) and Deardorff schemes (1kmD-NHM) were used for the turbulence closure scheme. The initial and boundary conditions were provided from the JMA mesoscale analysis data for 5km-, 2km-, 1km-, and 1kmD-NHM, and the results of 1km-NHM were used for the initial and boundary conditions in 500m- and 250m-NHM. In all experiments, the results were output at 10-minute intervals, and convection parameterization scheme was not used. Other setups were the same as those used by Saito et al. (2006).

Table 1. Description of the models.

	5km-NHM	2km-NHM	1km-NHM	1kmD-NHM	500m-NHM	250m-NHM
Horizontal grid spacing (m)	5000	2000	1000		500	250
Dimensions (x, y, z)	300×300×50	750×750×50	1500×1500×50		500×500×50	1000×1000×50
Integration time (JST)	12 JST on 26 - 15 JST on 27				21 JST on 26 - 15 JST on 27	
Turbulence closure scheme	Nakanishi and Niino (2004)			Deardorff (1980)		
Cloud microphysics scheme	Bulk cloud microphysics scheme with 2-moment cloud ice, snow, and graupel					

3. Representations of snowfall characteristics

Spatiotemporal variations of the cyclone and precipitation distributions were generally well reproduced by 5km-, 2km-, 1km-, and 1kmD-NHM (not shown), although the cyclone developed excessively in 1kmD- and 5km-NHM. Figure 1 shows elevations in each model and horizontal distributions of accumulated precipitation by snow from 12 JST (JST=UTC+9 h) on 26 to 15 JST on 27 March 2017 in the Mount Nasu region including Mt. Chausu, where the surface avalanche occurred in the southeastern side of the top. The terrain of the Mount Nasu was represented in all models, but the 5km-NHM did not resolve Mt. Chausu sufficiently. In the others, the detailed terrain was better represented as a smaller horizontal grid spacing. Although each model reproduced the localized heavy snowfall in the northeastern side of the Mount Nasu, only 500m- and 250m-NHM successfully reproduced the localized snowfall intensification close to the top of Mt. Chausu. Precipitation amount simulated by 1kmD-NHM was obviously larger than the others.

To verify the simulation results, precipitation amount at the JMA surface observation station of Nasu-kogen was compared with the results of simulations (Fig. 2). At the location of Nasu-kogen, precipitation type was almost all snow in any experiments. Although 1kmD- and 5km-NHM overestimated, the precipitation amount reproduced by the others agreed with the observation.

To investigate the differences of representation of snowfall characteristics in each model, vertical profiles averaged from 06 to 09 JST on 27 at the point of the windward (northeastern) side of the Mount Nasu were examined (Fig. 3). Firstly, updrafts at the altitude from 4 to 8 km in 1kmD- and 5km-NHM were greater than the others (Fig. 3a). Water vapor flux at the altitude from 3 to 4.5 km and mixing ratio of snow at any altitude in these experiments were also greater than the others (Fig. 3b). It is indicated that these differences were caused by representation of the cyclone development, resulting in overestimated snowfall amounts in 1kmD- and 5km-NHM.

Orographically forced updraft at the altitude from 1 to 2 km tended to get stronger as smaller horizontal grid spacing of models, and the representation of supercooled water cloud formed by the updrafts had the same characteristics (Fig. 3c). The low-level snowfall intensification at the altitude below 2 km were reproduced in 2km-, 1km-, 500m, and 250m-NHM (Fig. 3b), and the results of 500m- and 250m-NHM showed almost the same representation in the mixing ratio of cloud water in addition to snow.

These results indicate that model with a horizontal grid spacing equal to and smaller than 2 km is required for the representation of the low-level snowfall intensification associated with the orographic cloud seeding, although the localized snowfall distribution was also simulated in 5km-NHM. In this case, it is indicated that the formation of a weak layer in snowpacks associated with the difference of snowcrystal types was important for the occurrence of the surface avalanche in addition to short-duration heavy snowfalls (Araki, 2018). Therefore, the model with a horizontal grid spacing equal to and smaller than 500 m, which can explicitly represent the low-level snowfall intensification causing the modification of snowcrystal types, would be useful for the diagnosis of the potential of surface avalanches.

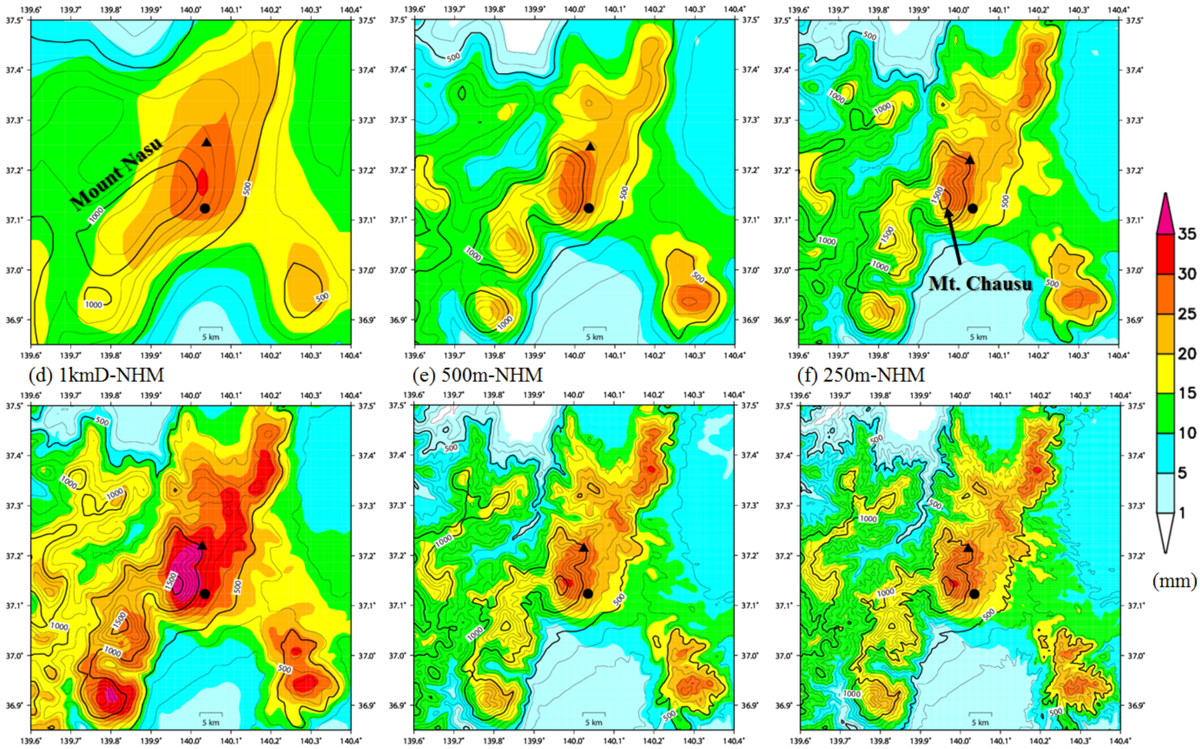

Figure 1. Horizontal distributions of accumulated precipitation of snow from 15 UTC on 26 to 06 UTC on 27 March 2017. Contour lines show elevations in each model. Black circle and triangle respectively indicate the location of the Nasu-kogen station and the analyzed point in Fig. 3.

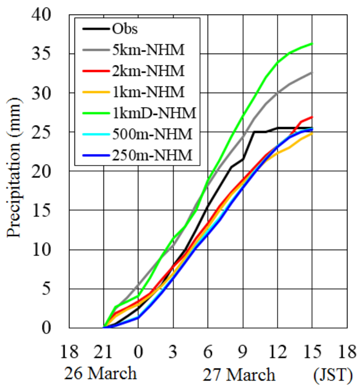

Figure 2. Precipitation amount derived from observation in Nasu-kogen (Obs) and each model.

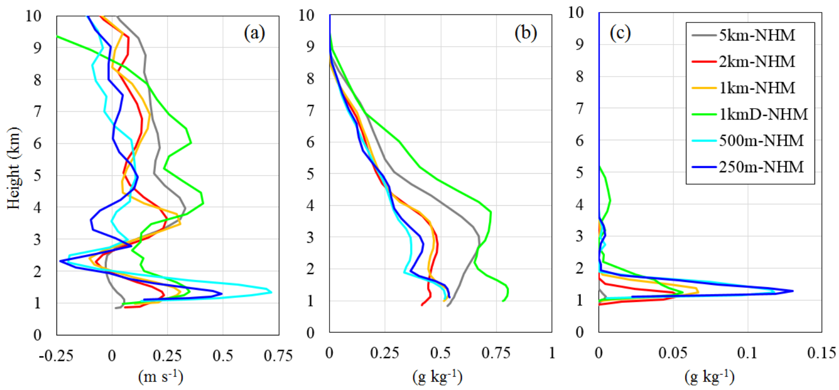

Figure 3. Profiles of (a) vertical velocity, (b) mixing ratio of snow, (c) mixing ratio of cloud water averaged from 06 to 09 JST on 27 at the windward (northeastern) side of Mt. Chausu (triangle in Fig. 1).

References:

Araki, K., 2018: Snowfall characteristics of heavy snowfall events associated with cyclones causing surface avalanche in Nasu, Japan. *Seppyo*, **80**, 131–147, (in Japanese with English abstract).

Big data and inverse problem for Ekman - Akerblom model

Philipp L.Bykov (1,2), Vladimir A. Gordin (2,1)

Hydrometeorological Center of Russia & National Research University Higher School of Economics

Moscow, Russia, vagordin@mail.ru

The Ekman - Akerblom model can be used to describe a velocity in the ocean or atmosphere boundary layer:

$$\begin{matrix} \partial_z k \partial_z u = l\left(v - v_g\right) \\ \partial_z k \partial_z v = -l\left(u - u_g\right) \end{matrix}, \quad z \in [0, H], \qquad u(0) = v(0) = 0,\; u(H) = u_g,\; v(H) = v_g \qquad (1)$$

where $\langle u(z), v(z) \rangle$ is the vertical profile of the horizontal flow, $\langle u_g, v_g \rangle$ is the geostrophic wind, l is the Coriolis parameter, and H is the boundary layer height. The turbulent exchange coefficient k in the approximate model of the boundary layer can be defined by various ways. Ekman (1905) and Akerblom (1908) used the simplest version: $k = const > 0$. Many various parameterizations for the coefficient $k(z)$ were considered during the next century assuming that k can depend on the coordinate z, on the temperature stratification $T(z)$, etc. In order to compare the skill of boundary layer parameterizations we could include them to a general atmospheric circulation model (GCM) and analyze its performance. However, finally the comparison results (which require long numerical experiments) may be depending on the GCM applied.

We introduce here an alternative approach: we suggest to use an archive of measurements with a good vertical resolution (obtained e. g. from radiosondes in BUFR code) and determine an “optimal” coefficient $k(z)$ by minimization of the residual of system (1). We integrate (1) with respect to z and introduce its residual. The averaged residual is the integral functional, and we minimize it:

$$I[k(z)] = \sum \frac{1}{H} \int_0^H \left\{ \left[k\partial_z u - l\int \left(v - v_g\right) dz + c_1 \right]^2 + \left[k\partial_z v + l\int \left(u - u_g\right) dz + c_2 \right]^2 \right\} dz \to \min_{k(z) \ge 0, c_1, c_2} . \quad (2)$$

Here we use the summation over a set of measured wind profiles. For the residual of relation (1), the variational approach gives the corresponding Euler equation and the transversality boundary conditions. If we search for $k(z)$ in the form of a piecewise linear function, then the minimization problem (2) is a quadratic programming problem with sparse matrix, and we can use classical numerical methods.

We can use an ansatz from the following: $k = k(z),\; k = k(z/H),\; k = k\left[\sqrt{(\partial_z u)^2 + (\partial_z v)^2}\right]$ etc for the minimization of (2). If the inequality $k(z) \ge 0$ is active during the minimization, i.e. the extremal $k(z)$ is not strongly positive, the restriction should be revised to provide a stronger minimization. If we obtain an extremal $k(z) \equiv 0$ that vanishes in some segment $\Delta \subset [0, H]$, and the solution $\langle u(z), v(z) \rangle$ of system (1) does not exist. We should modify system (1):

$$\partial_z \left[A\, \partial_z \begin{pmatrix} u \\ v \end{pmatrix} \right] = l \begin{pmatrix} u - u_g \\ v - v_g \end{pmatrix}, \; where\; A = \begin{pmatrix} \gamma(z) & -k(z) \\ k(z) & \gamma(z) \end{pmatrix}. \qquad (3)$$

This system has a smooth solution if $k^2 + \gamma^2 \ne 0$, and therefore we do not need the restriction $k(z) \ge 0$ any longer. Now we minimize the functional

$$\frac{1}{H}\sum\int_0^H\left\| A\partial_z\begin{pmatrix}u\\v\end{pmatrix}-l\int\begin{pmatrix}u-u_g\\v-v_g\end{pmatrix}dz+\begin{pmatrix}c_1\\c_2\end{pmatrix}\right\|^2 dz\to\min_{c_1,c_2,\gamma,k} \quad . \tag{4}$$

We defined (see e.g. [Troen and Mahrt 1986]) the height of the boundary layer H as the first root of equation

$$\Theta(H)=\Theta_V(0), \tag{5}$$

where Θ is the potential temperature and Θ_V is the potential virtual temperature. We only considered the profiles, where the root belonged to the interval $2000m > H > 200m$. The condition is fulfilled for 40% of the profiles (2665 radiosondes with mean height $H_{mean}=534m$). In Fig.1 we show the results of optimization for a) $k(z)\ge 0, \gamma(z)\equiv 0$. and b) k,γ - arbitrary. In case a) the mean error according to formula (4) for this evaluation is equal to $7.3\cdot 10^{-3} m^2/s$, while the correlation between left and right parts of system (3) is 21.6%. In case b) the mean error is $3.5\cdot 10^{-3} m^2/s$, and the correlation is 54.7%.

Results. If we substitute real wind profiles into the Ekman – Akerblom model there is a significant residual. We conjugate information about the real wind profiles with the Ekman – Akerblom model or its generalization. In case b) the optimal coefficient $k=k(z)$ is not strongly positive. The maximum of the new coefficient $\gamma(z)$ is substantially greater than the maximum of $k(z)$.

The article was prepared within the framework of the Academic Fund Program at the National Research University Higher School of Economics (HSE) in 2018 - 2019 (grant № 18-05-0011) and supported within the framework of a subsidy granted to the HSE by the Government of the Russian Federation for the implementation of the Global Competitiveness Program.

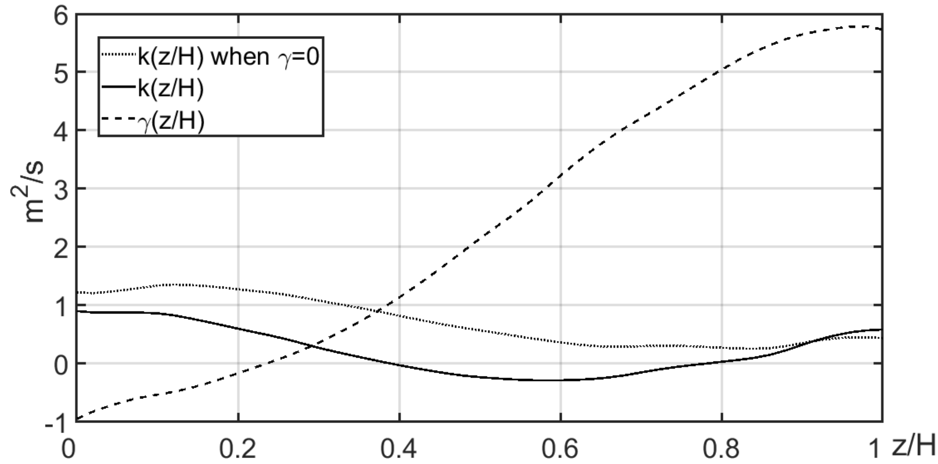

Fig.1. Optimal coefficients (in m^2s^{-1}) a) $\gamma(z/H)\equiv 0$; b) arbitrary functions $k(z/H)$, $\gamma(z/H)$

References

Akerblom F. Rechercher sur les courants le plus bas de l'atmosphere au-dessus de Paris. Nova Acta, Regic Societatis Scientarum. Upsala Ser. IV, V.2, №2, 1908, 203-251.

Ekman V. W. On the influence of the Earth's rotation on ocean currents. Arch. Math. Astron. Fysik., Bd.2, H.1/2 (№ 11), 1905. 1- 52.

Monin A.S., Yaglom A.M. Statistical Fluid Mechanics. V.1, Mechanics of Turbulence. Dover Books on Physics, 2007.

Troen I., Mahrt L., 1986: A simple model of the atmospheric boundary layer, Boundary-Layer Met. 37, 129-149.

PREP-CHEM-SRC VERSION 1.8: improvements to better represent local urban and biomass burning emissions over South America

Ariane Frassoni*, Daniela de Azeredo França*, Angel D. Chovert*, Fernanda Batista Silva*, Gabriel Pereira[o], Denis Eiras*, Valter Oliveira*, Saulo R. Freitas*, Karla Longo*, Marcelo Alonso[+]

*Center for Weather Forecasting and Climate Studies, Brazilian National Institute for Space Research, Cachoeira Paulista, SP, Brazil; [o]Federal University of São João del-Rei, MG, Brazil; [+]Federal University of Pelotas, RS, Brazil

1. Introduction

Atmospheric composition studies with numerical simulations have been widely conducted, motivated by the increasing computational resources and improvements in the representation of atmospheric-chemistry models (Freitas et al. 2011). The spatial and temporal distribution of emissions has a strong role in air quality forecast and is crucial information for numerical models. Better emission representation helps improving the skill of atmospheric–chemistry models as well as the global inventories commonly used to represent the most important primary atmospheric trace gases and aerosols. Since 2003, many improvements have been applied to the Air Quality Forecast System (AQFS) of the Center for Weather Forecasting and Climate Studies of the National Institute for Space Research in Brazil (CPTEC/INPE), which has the Brazilian developments on the Regional Atmospheric Modeling System (BRAMS) as the main component, resulting in successful air quality forecasts for South America. CPTEC/INPE develops the emission pre–processor called PREP-CHEM-SRC, a tool that provides emissions fields of trace gases and aerosols for the BRAMS-AQFS, as well as for other regional and global atmospheric chemistry models (Freitas et al. 2011). PREP-CHEM-SRC has been updated with improvements and implementations according to user needs. All implementations available in previous versions were merged in the new version called PREP-CHEM-SRC 1.8. In addition, new improvements were also developed. In this paper we present PREP-CHEM-SRC version 1.8 and discuss the main improvements available in this version, including updated Emission Factors (EFs) for biomass burning used in the Brazilian Biomass Burning Emission Model (Longo et al. 2010, 3BEM) and updates in urban emissions for Metropolitan Areas of São Paulo (MASP) and Rio de Janeiro (MARJ), following the methodology proposed by Alonso et al. (2010).

2. Biomass burning emissions

EFs of different chemical species were updated in the PREP-CHEM-SRC version 1.8 emissions code with specific information for South America. To this end, we proceed with the review, update and computation of EFs in spreadsheets. A wide bibliographic search regarding these parameters was carried out. The updated EFs were based in Andreae and Merlet (2001), Andreae (personal communication, 2016) and Yokelson et al. (2013). Finally, the estimated EFs were included in the source code of PREP-CHEM-SRC. The PREP-CHEM-SRC categories updated with EFs specific for South America (mainly Brazil) were: tropical forest, savanna, pasture/agricultural area and agricultural residues. Categories like extratropical forest, biofuel and charcoal burning were updated with EFs values of the world literature due to the lack of values for South America.

PREP-CHEM-SRC 1.8 was run by operating with fires detected by remote sensing information from the Geostationary Operational Environmental Satellite (GOES) data, Moderate Resolution Imaging Spectroradiometer (MODIS) and data operationally produced by the Division of Satellites and Environmental Systems (from the acronym in Portuguese for Divisão de Satélites e Sistemas Ambientais - DSA) at CPTEC/INPE from August through October 2015. The results indicated that both estimated total emissions of carbon monoxide (CO), nitrogen oxides (NOx) and methane (CH_4, Figure 1a) for South America did not change from previous versions compared with PREP-CHEM-SCR version 1.8 (Figure 1b), indicating the new version is functional. Experiments were also carried out using version 1.8 operating with fires and new EFs for the global scale, which generated equivalent results.

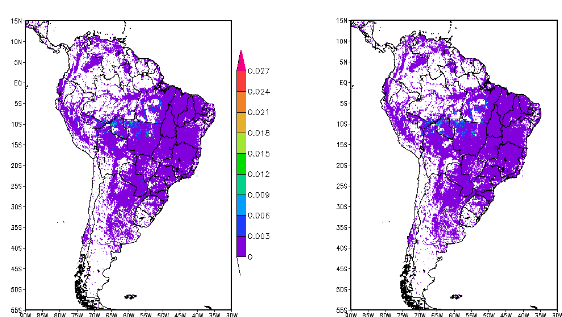

(a) (b)

Fig. 1. Comparison between CH_4 (kg/m^2) emissions from PREP-CHEM-SRC versions a) 1.6 and b) 1.8.

PREP-CHEM-SRC version 1.8 also takes into account the estimation of tracers and aerosols from biomass burning emissions by using the Fire Radiative Power (FRP) methodology available in version 1.6 (Pereira et al. 2009, 2016). The FRP is considered an indicator of the amount of biomass consumed or the emission rate of trace gases and aerosols released into the atmosphere at a burning event (Pereira et al. 2009). In order to compare differences between FRP and 3BEM emission estimation methods available in PREP-CHEM-SRC VERSION 1.8, a climate simulation with BRAMS version 5.2

* *Corresponding author address:* Ariane Frassoni, Center for Weather Forecasting and Climate Studies, Rodovia Presidente Dutra Km 40, Cachoeira Paulista, SP, Brazil
E-mail: ariane.frassoni@inpe.br

(Freitas et al. 2017) with 20km grid-spacing was carried out for August-September 2014, during the dry season in South America. Comparative differences are made to show how BRAMS Aerosol Optical Depth (AOD) simulations are sensitive to FRP and 3BEM emissions (Figure 2). As discussed in Pereira et al. (2016), FRP better represents smoke particle loading in the eastern region of Amazon forest compared with 3BEM, as well as in transition areas of Amazon rainforest and Brazilian savanna, like in central Brazil and west portion of Northeast Brazil both in August (Figure 2a) and September (Figure 2b). However, due drier conditions climatologically observed during September, such characteristics are highlighted. It is observed overestimation of AOD specially in central Brazil, and underestimation in western part of Amazon rainforest considering emissions estimated by FRP methodology (Figure 2).

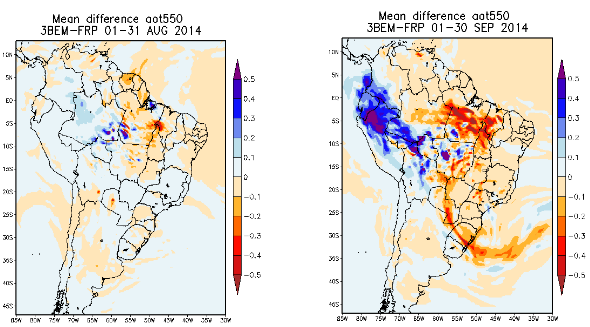

(a) (b)

FIG. 2. Difference between Aerosol Optical Depth simulations using a) 3BEM and b) FRP emissions generated by PREP-CHEM-SRC version 1.8.

3. Urban emissions

With public policies adopted in the São Paulo State aiming the reduction of pollution in urban areas, it has been observed decreasing emissions by vehicular fleet in MASP. Values applied in previous versions of PREP-CHEM-SRC were based on reports from the Environmental Company of the São Paulo State (CETESB) of 2005/2006.

In order to update the database for local urban emissions both in MASP and MARJ, the annual vehicle emission up to 2030 was determined for NOx and CO species for each city of the metropolitan areas using different scenarios. Geographic distribution of emissions was carried out using information of types of roads and traffic information for 2015 available in the National Department of Traffic (DENATRAN) website. Emission scenarios for NOx and CO in MARJ were extracted from Rosa (2011), while the values of total vehicular emission of pollutants for MASP municipalities were estimated from CETESB technical report published in 2015.

The methodology considered the analysis of the fleet by municipalities, determining the percentage that represents vehicles of the automobile category in each of the 39 municipalities of MASP and 92 municipalities in MARJ in relation to the total number for 2015. These information allowed the use of total annual emissions to weight emissions by municipalities in the regions according with the local fleet. By multiplying the value of the total annual vehicular emission of each species by the weight determined with the procedure described, an approximate annual vehicle emission value per municipality was obtained for each species. We selected automobile category considering that it has the largest number of units and exert important role on urban emissions. The method allowed the incorporation of the local emission data, making a homogeneous distribution by municipalities in MASP and MARJ. To include the industrial contributions to the emissions, the global datasets RETRO (REanalysis of TROpospheric chemical composition) and EDGAR-HTAP (Emission Database for Global Atmospheric Research) were used. Biogenic contributions took into account information from MEGAN (Model of Emissions of Gases and Aerosols from Nature) model.

4. Concluding remarks

The PREP-CHEM-SRC version 1.8 is presented. Emission factors for different biomes of South America were updated using bibliographic information. The methodology to estimate biomass burning emissions based on Fire Radiative Power is available in the present version. In addition, an update of urban emissions of Metropolitan Areas of São Paulo and Rio de Janeiro was included in PREP-CHEM-SRC version 1.8. Such improvements and new developments are of fundamental importance to better represent emissions in local and regional scale and add value to integrate databases of emission sources specially in areas with lack in local inventories. Better representation of emissions provide predictive skill on air quality forecasts. PREP-CHEM-SCR version 1.8 and previous releases are available on BRAMS homepage (http://brams.cptec.inpe.br/).

Acknowledgments. The authors thank São Paulo Research Foundation (FAPESP, project 2016/10137-1) for financial support.

References

Alonso, M. F., K. M. Longo, S. R. Freitas, R. M. da Fonseca, V. Marécal, M. Pirre, and L. G. Klenner, 2010: An urban emissions inventory for south america and its application in numerical modeling of atmospheric chemical composition at local and regional scales. *Atmospheric Environment*, **44 (39)**, 5072 – 5083, doi:https://doi.org/10.1016/j.atmosenv.2010.09.013, URL http://www.sciencedirect.com/science/article/pii/S1352231010007673.

Andreae, M., and P. Merlet, 2001: Emission of trace gases and aerosols from biomass burning. *Global Biogeochemistry Cycles*, **15**, 955–966.

Freitas, S. R., and Coauthors, 2011: Prep–chem-src–1.0: a preprocessor of trace gas and aerosol emission fields for regional and global atmospheric chemistry models. *Geoscientific Model Development*, **4**, 419–433.

Freitas, S. R., and Coauthors, 2017: The brazilian developments on the regional atmospheric modeling system (brams 5.2): an integrated environmental model tuned for tropical areas. *Geoscientific Model Development*, **10 (1)**, 189–222, doi:10.5194/gmd-10-189-2017, URL https://www.geosci-model-dev.net/10/189/2017/.

Longo, K. M., S. R. Freitas, M. O. Andreae, A. Setzer, E. Prins, and P. Artaxo, 2010: The coupled aerosol and tracer transport model to the brazilian developments on the regional atmospheric modeling system (catt-brams) – part 2: Model sensitivity to the biomass burning inventories. *Atmospheric Chemistry and Physics*, **10 (13)**, 5785–5795, doi:10.5194/acp-10-5785-2010, URL https://www.atmos-chem-phys.net/10/5785/2010/.

Pereira, G., S. R. Freitas, E. C. Moraes, N. J. Ferreira, Y. E. Shimabukuro, V. B. Rao, and K. M. Longo, 2009: Estimating trace gas and aerosol emissions over south america: Relationship between fire radiative energy released and aerosol optical depth observations. *Atmospheric Environment*, **43 (40)**, 6388 – 6397, doi:https://doi.org/10.1016/j.atmosenv.2009.09.013, URL http://www.sciencedirect.com/science/article/pii/S135223100900778X.

Pereira, G., R. Siqueira, N. Rosário, K. Longo, S. R. Freitas, F. S. Cardozo, J. W. Kaiser, and M. J. Wooster, 2016: Assessment of fire emission inventories during the south american biomass burning analysis (sambba) experiment. *Atmospheric Chemistry and Physics (Online)*, **16**, 6961–6975.

Rosa, L. P., 2011: Inventário de emissões atmosféricas por veículos automotores do estado do rio de janeiro. Tech. rep., Programa de Engenharia de Transportes - PET/COPPE/UFRJ, Rio de Janeiro, RJ.

Yokelson, R. J., and Coauthors, 2013: Coupling field and laboratory measurements to estimate the emission factors of identified and unidentified trace gases for prescribed fires. *Atmospheric Chemistry and Physics*, **13**, 89–116.

An evaluation of the Energy budget computed with observed Enthalpy surface fluxes.

by Pascal Marquet[(1)], Guylaine Canut[(2)] and William Maurel[(2)]

Météo-France. [(1)]CNRM/GMAP. [(2)]CNRM/GMEI. Toulouse. France. *E-mail: pascal.marquet@meteo.fr*

1 Motivations - Introduction.

The energy budget of the atmosphere simulated by GCM or NWP models is currently monitored with the aim of having closed values for the "surface energy budget". However, it is explained in Marquet (2015a,b) that the way the surface fluxes of sensible (temperature) and latent (water) energies are computed is still a subject of debate, and in particular for the latent heat flux.

In the present study, the new moist-air enthalpy fluxes derived in Marquet (2015b) are evaluated and compared to the usual (standard) ones based on the latent heats of vaporization or sublimation. This evaluation is made by using the observation datasets of the Météopole-Flux observatory located at the CNRM, Toulouse, France.

2 The moist surface energy flux.

The simple case of no condensed water will be considered in this study, and the moist air is thus composed only of dry air and water vapor.

According to Marquet (2015a,b), the energy flux at the bottom of the atmosphere is computed by $F_h \approx \overline{\rho}\;\overline{w'\,h'}$, where the overbar means Reynolds averaging, primed values refer to fluctuations, and h is the thermal enthalpy given by

$$h \;=\; h_{\rm ref} \;+\; c_{pd}\,T \;+\; L_h\,q_v \,, \qquad (1)$$

$$\text{where} \quad L_h\,(T) \;=\; h_v(T) \;-\; h_d(T)\,, \qquad (2)$$

$h_{\rm ref}$ is a constant reference value, and q_v is the specific content of water vapor. The difference in enthalpies $L_h(T) = (c_{pv}-c_{pd})\,(\,T-T_r\,) + L_h(T_r)$ is computed with $L_h(T_r) = (h_v)_r - (h_d)_r = 2603$ kJ/kg at $T_r = 273.15$ K. The difference of specific heats at constant pressure for water vapor and dry air is $c_{pv} - c_{pd} = 1846.1 - 1004.7 = 841.4$ J/K/kg.

The turbulent flux of h is equal to

$$F_h \;=\; \overline{\rho}\;c_p\;\overline{w'\,T'} \;+\; \overline{\rho}\;L_h(T)\;\overline{w'\,q'_v} \;, \qquad (3)$$

where c_p is the moist-air value $(1-q_v)\;c_{pd} + q_v\;c_{pv}$. This flux of enthalpy F_h is thus different from the usual sensible (SH) plus latent (LH) heat fluxes given by

$$SH + LH \;=\; \overline{\rho}\;c_p\;\overline{w'\,T'} \;+\; \overline{\rho}\;L_v(T)\;\overline{w'\,q'_v} \;, \qquad (4)$$

where the latent heat of vaporization is $L_v(T) = L_v(T_r) + (c_{pv} - c_l)\,(\,T - T_r\,)$, with $L_v(T_r) = (h_v)_r - (h_l)_r = 2501$ kJ/kg and $c_{pv} - c_l = 1846 - 4218 = -2372$ J/K/kg, where c_l is the specific heat at constant pressure of liquid water.

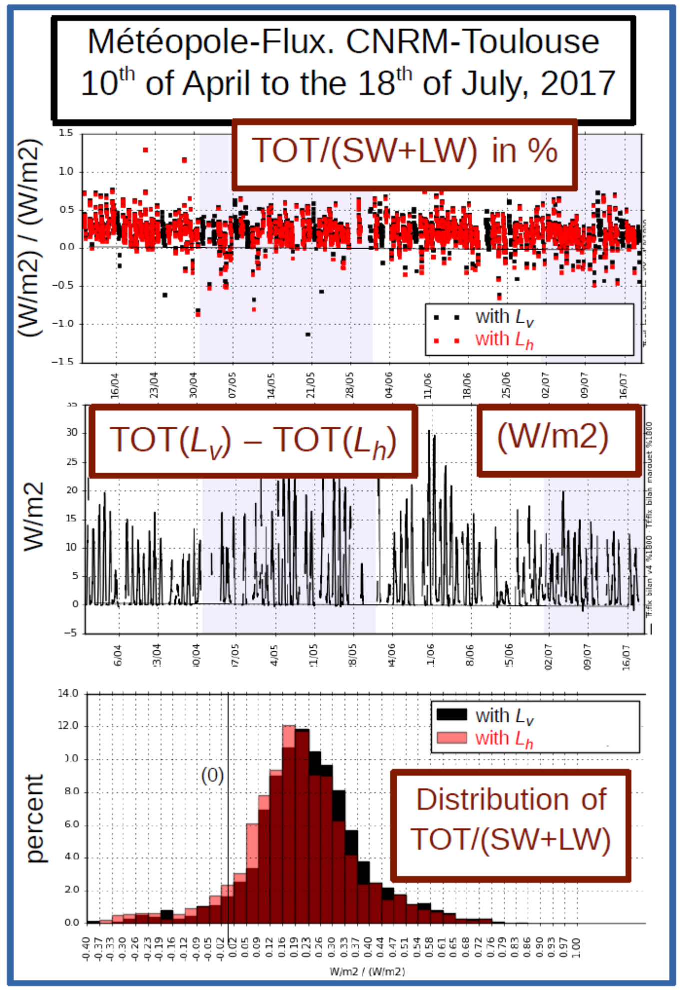

Figure 1: *The formulations with $L_v(T)$ and $L_h(T)$ are compared for a period of 100 days: the relative impact with respect to $SW + LW$ (top); the difference of total budgets (center); the distribution of the relative impact (bottom).*

It is shown in Marquet (2015b) that $L_h(T)$ is about 4 % to 8 % larger than $L_v(T)$, depending on T. Therefore, the latent heat flux computed with $L_h(T)$ in Eq.(3) is expected to be about 6 % larger than the usual one computed with $L_v(T)$ in Eq.(4).

3 Numerical evaluations.

The Météopole-Flux dataset is described in the web site `https://www.umr-cnrm.fr/spip.php?article874&lang=en`. Daily reports are available at `http://www.umr-cnrm.fr/data/FL_1jour.png` and

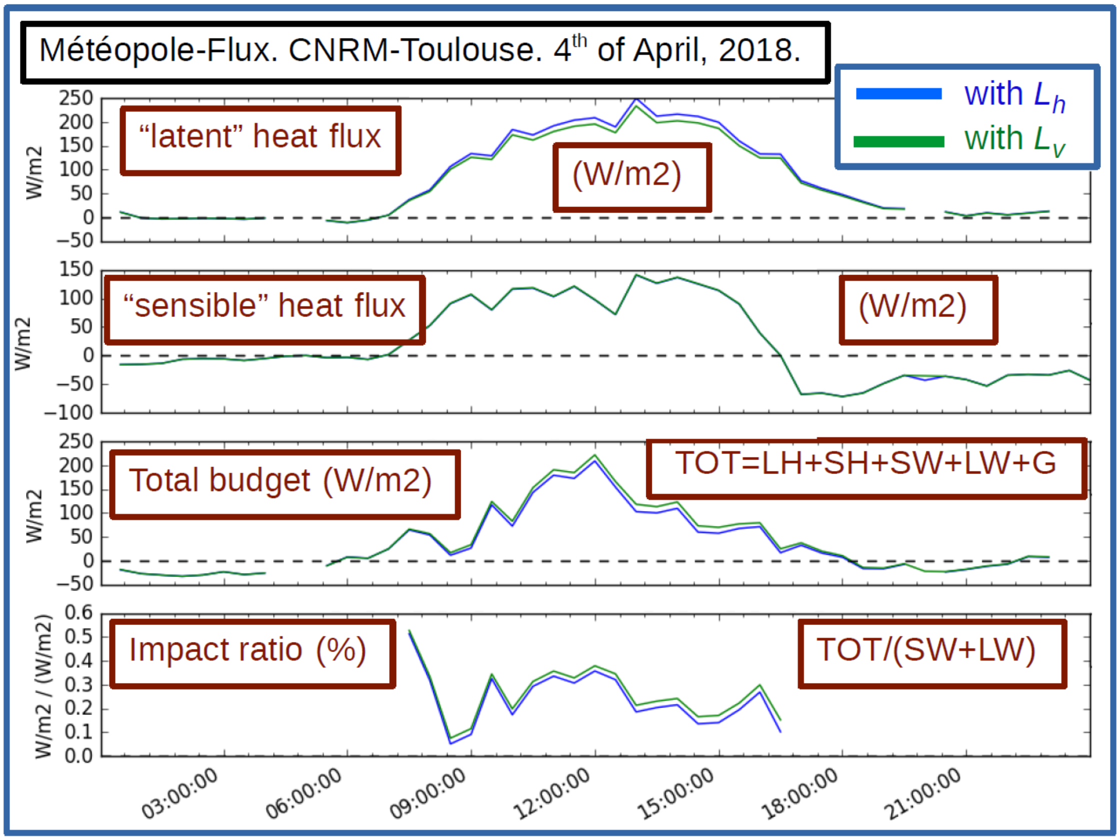

Figure 2: *The energy budgets at the Météopole-Flux site and for one particular day (the 4th of April 2018). The formulations with $L_v(T)$ (in green) or $L_h(T)$ (in blue) are compared (from the top to the bottom) for: the latent heat fluxes; the sensible heat fluxes; the total budgets; the relative impact in comparison with the net radiative fluxes.*

`http://www.umr-cnrm.fr/data/ST_ARP_ARO_7J.pdf`

The turbulent fluxes of temperature and water are observed at the Météopole-Flux by using an eddy-correlation method with 2D-rotation and high-band running-mean filter. The instruments are installed on a mast at 3.70 m above the ground level. Three wind components (u, v, w) and the sonic temperature (T) are measured at 20 Hz with a Gill Windmaster Pro sonic anemometer. A Licor-7500 hygrometer measures water vapor concentration at 20 Hz. Mean absolute temperature and humidity are measured with PT100 and Vaisala HMP110 instruments located in a shield.

Three HFP01 plates (Hukseflux Thermal Sensors) are used to compute the ground flux G as a mean value over three areas of 1 m^2, in order to reduce the variability in space. The heat flux plates are placed at 5 cm soil depth. These sensors are used extensively by the community to measure G in surface energy budgets.

Fig.1 shows, for a period of 100 days, an evaluation of the impact on the energy balance of using F_h in place of the classical sum $SH + LH$. The residual energy is globally decreased by about 3 to 4 % when $L_h(T)$ is taken into account, with a resulting improved total energy budget $TOT = SH + LH + SW + LW + G$, where $SW + LW$ is the net radiative flux, and G is the ground flux.

For one day measurements, Fig.2 shows that the latent heat flux calculated with $L_h(T)$ is slightly greater (about +6 %) than the one calculated with $L_v(T)$ during the day (between 09 UTC and 18 UTC). The change for the sensible heat flux is very small.

4 Conclusions.

The expected impact of about +6 % of LH is observed for the new latent heat flux computed with $L_h(T)$, in comparison with the usual one computed with $L_v(T)$. The difference in energy budget can reach 15 to 30 W/m^2 on some days. However, the average decrease of the imbalance in surface energy budget observed at the Météopole-Flux site is small, and a significant imbalance still exists which cannot be explained by the errors in computing the latent heat flux.

References

• P. Marquet (2015). On the computation of moist-air specific thermal enthalpy. *Q. J. R. Meteorol. Soc.* **141** (686): p.67–84. `https://arxiv.org/abs/1401.3125`

• P. Marquet (2015). Definition of Total Energy budget equation in terms of moist-air Enthalpy surface flux. *CAS/JSC WGNE Research Activities in atmospheric and oceanic modelling*, WCRP Report No.12, pp. 4-16-4-17. Available online at `http://bluebook.meteoinfo.ru/uploads/2015/individual-articles/04_Marquet_Pascal_h_Flux.pdf`

Sensitivity of the prediction of Typhoon Lionrock (2016) to the parameter in the cloud scheme using the 7-km mesh nonhydrostatic global spectral atmospheric Double Fourier Series Model (DFSM)

Akiyoshi Wada*, Hiromasa Yoshimura and Masayuki Nakagawa
Meteorological Research Institute, Tsukuba, Ibaraki, 305-0052, JAPAN
*awada@mri-jma.go.jp

1. Introduction

This report is similar to Wada et al. (2018) except that this examination addresses the sensitivity of the prediction of a storm to the parameter in the cloud scheme of the 7-km mesh nonhydrostatic global spectral atmospheric Double Fourier Series Model (DFSM). As described in Wada et al. (2018), the over-intensification was found in the prediction of the intensity of Typhoon Lionrock (2016). The purpose of this study is to understand the sensitivity of the prediction of Lionrock to the parameter associated with the cloud diagnosis in DFSM. This process is considered to be as important as surface boundary processes because it is closely related to diabatic heating within the inner core of the storm.

2. Experimental design

The experimental design is almost the same as in Wada et al. (2018) except for the kind of sensitivity experiments. That is, the initial time of the prediction of Lionrock is set to 0000 UTC 23 August 2016. The prediction period is from this initial time to 0000 UTC 31 August 2016. The integration time is 8 days. The specification of the original DFSM is the same as in Table 4 of Nakano et al. (2017). The experiment name 'DFSM' represents 'DFSM_nolimevp' in Wada et al. (2018): The threshold regarding the limitation of the evaporation in the cloud scheme is not considered. The package of physical schemes incorporated into the DFSM is based on GSM1403. The cloud parameter 'cwcadd' represented the supplement amount of cloud water content, which was originally adjusted to mitigate the time step dependence of predicted precipitation due to large scale condensation in GSM1403 with the horizontal resolution corresponding to 20 km. 'Qs' indicates saturated specific humidity. In a series of the experiments 'Modify', the effect of the gust was removed. Instead, the effect of sea spray on turbulent heat fluxes (Bao et al., 2000) was incorporated into the DFSM. The inclusion of the Bowen ratio (0.1) as estimating the upper limit of sensible heat fluxes against latent heat fluxes is the same as in Wada et al. (2018). Thus, all the four numerical prediction experiments shown in Table 1 were performed using the DFSM.

Table 1 List of sensitivity numerical prediction experiments for the prediction of Lionrock

Experiment name	Cloud parameter	Gust	Sea spray	Limitation of Bowen ratio (0.1)
DFSM	Min(cwcadd, 0.3*Qs)	○	×	×
DFSM_Modify_03	Min(cwcadd, 0.3*Qs)	×	○	○
DFSM_Modify_02	Min(cwcadd, 0.2*Qs)	×	○	○
DFSM_Modify_01	Min(cwcadd, 0.1*Qs)	×	○	○

3. Results

3.1 Track prediction

Figure 1 shows the results of track predictions in four experiments (Table 1) and the Regional Specialized Meteorological Center (RSMC) Tokyo best track. In the DFSM experiment, the predicted storm moved southwestward and changed the direction to eastward north of the best-track recurvature point (Wada et al., 2018). After the recurvature, the storm moved more eastward compared with the RSMC Tokyo best track. The cloud parameter 'cwcadd' did affect the track prediction clearly. When the effect of saturated specific humidity on the supplement amount of cloud water content reduced, the predicted storm tended to move more slowly after the recurvature. However, the moving direction of the predicted storm was not simply explained by the value of the cloud parameter. This suggests that atmospheric environments associated with the steering flow did change due to the cloud parameter. In the following subsection, we will show the results of intensity predictions and predicted precipitation patterns to examine the effect on the track prediction.

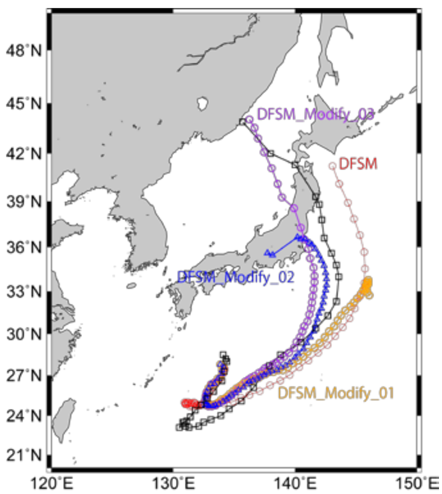

Figure 1 Results of track predictions

3.2 Intensity prediction

Figure 2 shows the results of intensity predictions compared with the RSMC best track intensity. Unlike the results in Wada et al. (2018), there was only a little difference in predicted central pressures and maximum wind speeds at 20 m height among the DFSM_Modify_01, DFSM_Modify_02 and DFSM_Modify_03 experiments. This implies that the difference of the intensity predictions was not crucial for explaining the difference of the track predictions among the three experiments. On the other hand, the difference of the intensity predictions found in the latter integration can be explained by the difference of the track predictions: In the DFSM_Modify_01 experiment, the intensity tended to be strong because the predicted storm was over the ocean during the integration, while the storm intensity tended to weaken due to making landfall in the main island of Japan.

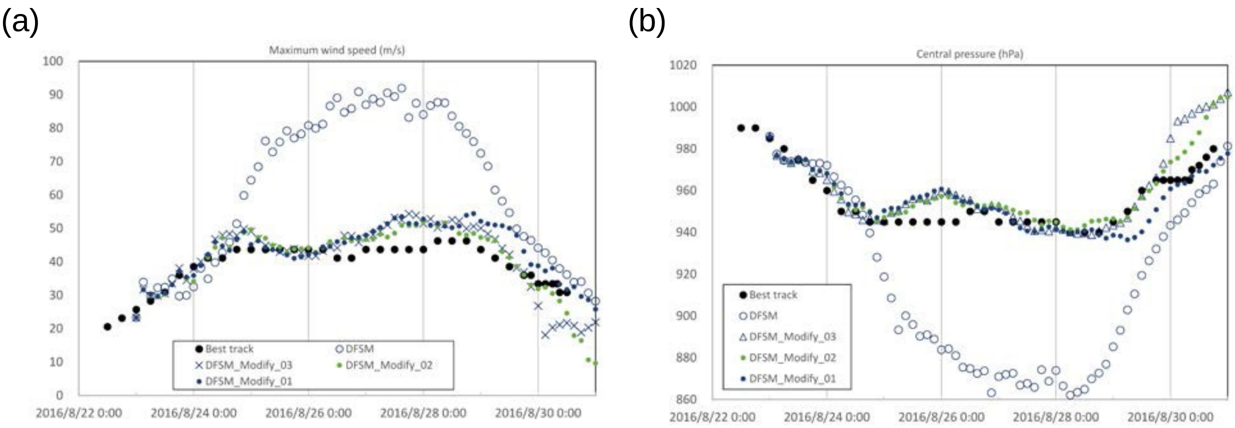

Figure 2 Time series of (a) predicted maximum wind speed at 10 m height and (b) predicted central pressure together with RSMC Tokyo best track data.

3.3 Precipitation pattern

Figures 3 and 4 show the horizontal distributions of precipitation rate and total precipitable water at 0000 UTC 27 August 2016, corresponding to 96-hour integration time. The wave-1 asymmetric pattern of precipitation rate (Fig. 3) was commonly found in the DFSM_Modify_03, DFSM_Modify_02 and DFSM_Modify_01 experiments. The horizontal distribution of total precipitable water, however, showed axisymmetric (Fig. 4) although the total precipitable water was locally high on the right side from the storm center in the DFSM_Modify_01 experiment. The similarity of the inner core structure of simulated storm was consistent with the results of intensity predictions.

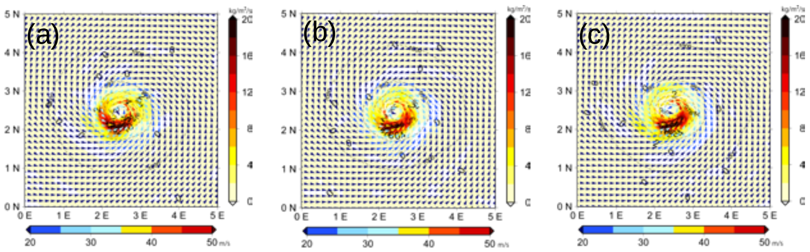

Figure 3 Horizontal distributions of precipitation rate (shades) collocated at the predicted storm center in the (a) DFSM_Modify_03, (b) DFSM_Modify_02 and (c) DFSM_Modify_01 experiments at 96 h. Arrows with colors indicate the surface wind vectors and speeds.

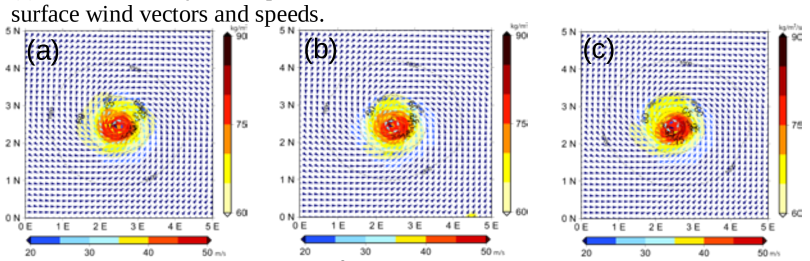

Figure 4 Same as Figure 3 except for total precipitable water.

4. Concluding remarks

The cloud parameter ‘cwcadd’ affected the track predictions of Lionrock (2016). However, this is a result of a single tropical cyclone case. Thus, we need to do sensitivity experiments for more tropical cyclone cases. In addition, we need to study how the atmospheric environments change due to the tuning of the cloud parameter.

References

Bao, J., J.M. Wilczak, J. Choi, and L.H. Kantha, 2000: Numerical Simulations of Air–Sea Interaction under High Wind Conditions Using a Coupled Model: A Study of Hurricane Development. Mon. Wea. Rev., 128, 2190–2210, https://doi.org/10.1175/1520-0493(2000)128<2190:NSOASI>2.0.CO;2

Nakano, M., Wada, A., Sawada, M., Yoshimura, H., Onishi, R., Kawahara, S., Sasaki, W., Nasuno, T., Yamaguchi, M., Iriguchi, T., Sugi, M., and Takeuchi, Y. (2017). Global 7 km mesh nonhydrostatic Model Intercomparison Project for improving TYphoon forecast (TYMIP-G7): experimental design and preliminary results, Geosci. Model Dev., 10, 1363-1381, https://doi.org/10.5194/gmd-10-1363-2017.

Wada, A, H. Yoshimura and M. Nakagawa, 2018: Sensitivity of the prediction of Typhoon Lionrock (2016) to the parameter in the surface boundary scheme using the 7-km mesh nonhydrostatic global spectral atmospheric Double Fourier Series Model (DFSM). CAS/JSC WGNE Res. Activities in Atm. And. Oceanic Modelling. Rep. 48, pp.4.05-4.06.

Acknowledgements

This work was supported by JSPS KAKENHI Grant Number JP15K05292.

Sensitivity of the prediction of Typhoon Lionrock (2016) to the surface boundary scheme using the 7-km mesh nonhydrostatic global spectral atmospheric Double Fourier Series Model (DFSM)

Akiyoshi Wada*, Hiromasa Yoshimura and Masayuki Nakagawa
Meteorological Research Institute, Tsukuba, Ibaraki, 305-0052, JAPAN
*awada@mri-jma.go.jp

1. Introduction

The Global 7 km mesh nonhydrostatic Model Intercomparison Project for improving TYphoon forecast (TYMIP-G7) is designed to understand and statistically quantify the advantages of high-resolution nonhydrostatic global atmospheric models to improve tropical cyclone (TC) prediction (Nakano et al., 2017). Through TYMIP-G7, we found that the central pressure in the 7-km mesh nonhydrostatic global spectral atmospheric Double Fourier Series Model (DFSM) showed over-intensification compared with that predicted by the Global Spectral Model (GSM) with a horizontal resolution corresponding to 20 km. Because both DFSM and GSM had the same specifications except for the horizontal resolution, this result suggests that the improvement of physics schemes suitable for such high-resolution models is needed for accurate forecasts of the central pressure. The over-intensification was also found in the prediction of Typhoon Lionrock (2016). The purpose of this study is to understand the sensitivity of the prediction of Lionrock to the surface boundary scheme in DFSM, which is closely related to diabatic heating within the inner core of the storm.

2. Experimental design

The initial time of the prediction of Lionrock is set to 0000 UTC 23 August 2016. The prediction period is from this initial time to 0000 UTC 31 August 2016. The integration time is 8 days. The specification of the original DFSM is the same as in Table 4 of Nakano et al. (2017). The first experiment name is 'DFSM_nolimevp', where 'nolimevp' means that the threshold regarding the limitation of the evaporation in the cloud scheme is not considered. The package of physical schemes incorporated into the original DFSM is the same as in GSM1403, while GSM1705 includes another package of physical schemes used in operational runs of GSM. The name of the corresponding experiment with the new physics is 'DFSM_GSM1705'.

In the original GSM1403 and GSM1705, the effect of gusts is considered to calculate air-sea momentum and turbulent heat fluxes. In the 'DFSM_nolimevp_Modify' experiment, the effect of gusts was neglected. Instead, the effect of sea spray on turbulent heat fluxes (Bao et al., 2000) was incorporated into the DFSM. In addition, the Bowen ratio (0.1) was used to limit the overestimation of sensible heat fluxes against latent heat fluxes. In other words, the upper limit of air-sea sensible heat fluxes was determined by using the Bowen ratio and latent heat fluxes. Thus, all the three sensitivity numerical prediction experiments shown in Table 1 were performed by using the DFSM incorporating the package of physical schemes used in GSM1403 / GSM1705.

Table 1 List of sensitivity numerical prediction experiment for the prediction of Lionrock

Experiment name	Model & Horizontal resolution	Gust	Sea spray	Limitation of Bowen ratio (0.1)
DFSM_nolimevp	7km GSM1403	○	×	×
DFSM_nolimevp_Modify	7km GSM1403	×	○	○
DFSM_GSM1705	7km GSM1705	○	×	×

3. Results

3.1 Track prediction

Figure 1 shows the results of track predictions in three experiments and the Regional Specialized Meteorological Center (RSMC) Tokyo best track. In the DFSM_nolimexp experiment, the predicted storm moved southwestward and changed the direction to eastward north of the best- track recurvature point. After the recurvature, the storm moved more eastward compared with the RSMC Tokyo best track. In the DFSM_nolimexp_Modify experiment, the track changed a little before arriving at the recurvature point. However, the moving direction changed after the recurvature and the predicted storm track tended to move westward compared with the RSMC best track and made landfall in Ibaraki prefecture, south of the real landfalling location of the storm. In the DFSM_GSM1705 experiment, the predicted storm track was close to the track in the DFSM_nolimexp_Modify experiment although the moving speed became slower.

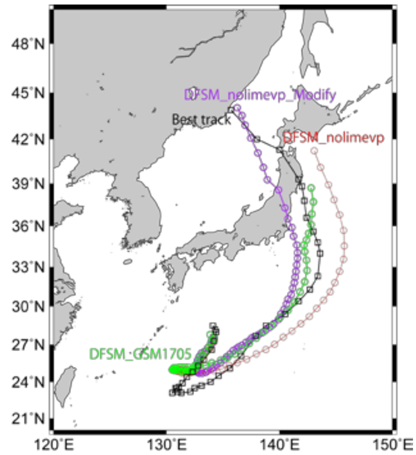

Figure 1 Results of track predictions

3.2 Intensity prediction

Figure 2 shows the results of intensity predictions compared with the RSMC best track intensity. In Figure 2a, the maximum wind speed at 10 m height in the DFSM_nolimevp experiment was much higher than that in the other experiments and the best track maximum wind speed at 10 m height. Unlike the simulated central pressures, the maximum wind speeds in the DFSM_nolimevp_Modify and DFSM_GSM1705 experiments were reasonably close to the best track maximum wind speed. In Figure 2b, however, predicted central pressure in the DFSM_GSM1705 experiment was much lower than that in the DFSM_nolimevp_Modify experiment and the best-track central pressure. This reveals that the wind-pressure relation in the DFSM_GSM1705 experiment strongly differed from the relation in the other two experiments and in the RSMC Tokyo best track data.

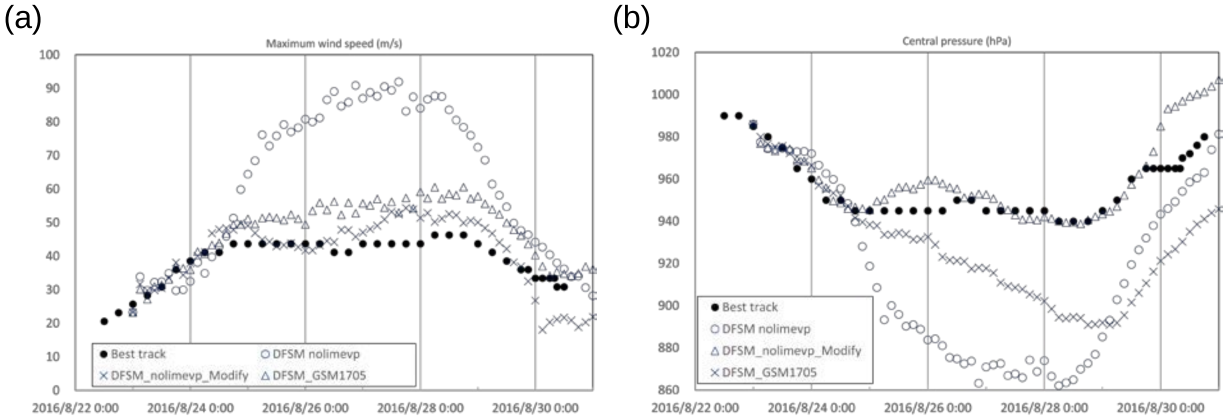

Figure 2 Time series of (a) predicted maximum wind speed at 10 m height and (b) predicted central pressure together with RSMC Tokyo best track data.

3.3 Sensible and latent heat fluxes

Figures 3 and 4 shows the horizontal distributions of sensible and latent heat fluxes at 0000 UTC 25 August 2016, corresponding to 48-hour integration time. In the DFSM_nolimexp experiment, the value of both sensible and latent heat fluxes within the inner core of the predicted storm was extremely high. The value of latent heat flux was relatively high, while the value of sensible heat flux within the inner core reduced clearly in the DFSM_nolimexp_Modify experiment due to the Bowen ratio limitation and the effect of sea spray scheme. In the DFSM_GSM1705, the value of latent heat flux was relatively low, while the value of sensible heat flux was relatively high.

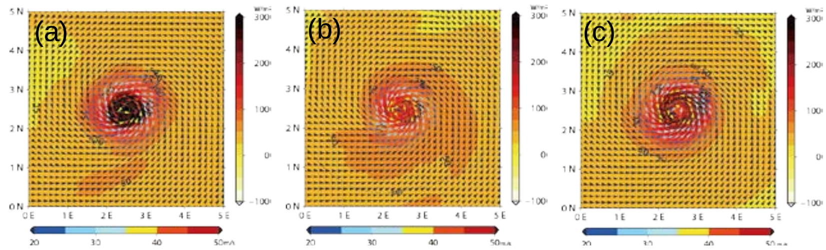

Figure 3 Horizontal distributions of sensible heat fluxes (shades) collocated at the predicted storm center in the (a) DFSM_nolimevp, (b) DFSM_nolimevp_Modify and (c) DFSM_GSM1705 experiments. Arrows with colors indicate the surface wind vectors and speeds.

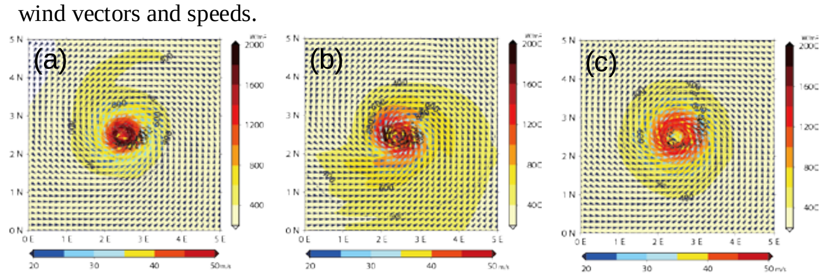

Figure 4 Same as Figure 3 except for latent heat fluxes.

4. Concluding remarks

The relation of the sensible and latent turbulent heat fluxes to predicted central pressures (Fig. 2b) was not straightforward. Although the latent heat flux around the inner-core of the storm was smallest, the predicted central pressure could become deeper. In other words, a large amount of turbulent latent heat flux within the inner core of the storm does not always contribute to deepen the central pressure of the storm because of the combination of physical schemes incorporated into the DFSM.

References

Bao, J., J.M. Wilczak, J. Choi, and L.H. Kantha, 2000: Numerical Simulations of Air–Sea Interaction under High Wind Conditions Using a Coupled Model: A Study of Hurricane Development. Mon. Wea. Rev., 128, 2190–2210, https://doi.org/10.1175/1520-0493(2000)128<2190:NSOASI>2.0.CO;2

Nakano, M., Wada, A., Sawada, M., Yoshimura, H., Onishi, R., Kawahara, S., Sasaki, W., Nasuno, T., Yamaguchi, M., Iriguchi, T., Sugi, M., and Takeuchi, Y. (2017). Global 7 km mesh nonhydrostatic Model Intercomparison Project for improving TYphoon forecast (TYMIP-G7): experimental design and preliminary results, Geosci. Model Dev., 10, 1363-1381, https://doi.org/10.5194/gmd-10-1363-2017

Acknowledgements

This work was supported by JSPS KAKENHI Grant Number JP15K05292.